Microstructure and bio-corrosion behavior of Mg–Zn and Mg–Zn–Ca alloys for biomedical applications

H. R. Bakhsheshi-Rad*, E. Hamzah, A. Fereidouni-Lotfabadi,
M. Daroonparvar, M. A. M. Yajid, M. Mezbahul-Islam,
M. Kasiri-Asgarani and M. Medraj

The microstructure and bio-corrosion behavior of binary Mg–xZn ($x = 1.25$, 2.5, 4) and ternary Mg–Ca–xZn ($x = 1.25$, 2.5, 4) alloys have been studied using scanning electron microscopy (SEM), electrochemical, and immersion tests. Microstructure analysis indicated that the binary Mg–Zn alloys are composed of primary α-Mg matrix and $Mg_{12}Zn_{13}$ phases, while, ternary Mg–Ca–Zn alloys are composed of α-Mg, Mg_2Ca, and IM1 ($Ca_3Mg_xZn_{15-x}$) ($4.6 \leq x \leq 12$) phases or α-Mg, IM1 and IM3 ($Ca_2Mg_5Zn_{13}$) phases. Electrochemical results showed that Mg–4Zn alloy has lowest corrosion rate among binary alloys. At constant Ca content of 0.8 wt.%, the addition of Zn up to 1.25 wt.% decreased the corrosion rate, while further addition of Zn increased the corrosion rate of ternary alloys. Immersion tests results demonstrated that the formation of Zn oxide layer in binary Mg–Zn alloy and evolution of eutectic phase (α-Mg + IM1 + Mg_2Ca) significantly retard the bio-degradation rate of the ternary alloys.

1 Introduction

Magnesium (Mg) has attracted great attention as a bio-degradable material suitable for implant applications as it can be gradually dissolved, absorbed, consumed, or excreted through the urine [1,2]. Furthermore, the release of Mg^{2+} ions into the body leads to the growth of new bone tissue and shorter healing time. Mg also has good bio-compatibility, low density, high specific strength [3] and its elastic modulus is similar to natural bone which helps to blunt the stress shielding effect [4]. However, Mg alloy applications are limited due to poor corrosion resistance, the release of hydrogen gas and high degradation rate when exposed to human body fluid [5–8]. These characteristics lead to a decline in the mechanical properties of pure Mg before new tissues are properly and adequately healed. Alloying is one of the main tools to enhance the corrosion

H. R. Bakhsheshi-Rad, E. Hamzah, A. Fereidouni-Lotfabadi,
M. Daroonparvar, M. A. M. Yajid
Department of Materials, Manufacturing and Industrial Engineering, Faculty of Mechanical Engineering, Universiti Teknologi Malaysia, 81310 Johor Bahru, (Malaysia),
E-mail: rezabakhsheshi@gmail.com, bhamidreza2@live.utm.my

M. Mezbahul-Islam, M. Medraj
Department of Mechanical Engineering, Concordia University, 1455 De Maisonneuve Blvd. West, Montreal, QC (Canada H3G 1M8)

M. Kasiri-Asgarani
Materials Engineering Department, Najafabad Branch, Islamic Azad University, Najafabad, Isfahan, (Iran),

resistance of Mg alloys [4,9,10]. Among the Mg alloy systems, Mg–Ca and Mg–Zn have shown a good combination of mechanical properties and corrosion behavior suitable for biomedical applications [11–13]. Calcium is one of the main elements in human bone and the release of Mg and Ca ions may improve the bone healing process [11,14]. Zn is known to increase age hardening response as it produces intermetallic compounds and refines the grain size [12,15]. A small amount of Zn contributes to overall strength due to solid solution and precipitation strengthening [13]. All previous studies acknowledge the improvement of corrosion resistance and mechanical properties of Mg via Ca and Zn addition and support the great potential of these alloys for implant applications. However, there is a lack of information concerning the influence of Zn content on the microstructure and corrosion resistance of binary Mg–Zn and ternary Mg–Zn–Ca alloys. In addition, the relationship between solidification behavior and corrosion rate have not been reported elsewhere. In the current study, the microstructure, solidification behavior and degradation behavior in simulated body fluid (SBF) of pure Mg and Mg–xZn ($x = 1.25$, 2.5, 4 wt.%) have been investigated and compared with the Mg–0.8Ca–xZn ($x = 1.25$, 2.5, 4 wt.%) alloys.

2 Experimental

Magnesium alloys were prepared by melting pure magnesium ingots of 99.99%, pure zinc chips (99.99%) and Mg–32Ca master alloy. The materials were melted by electrical resistance furnace

under an argon gas atmosphere in a mild steel crucible at 750 °C. The molten metal was maintained for around 45 min at the melting condition for stabilization. After stabilizing, molten alloy with different Zn contents (1.25, 2.5, and 4 wt.%) and constant 0.5 wt.% Ca concentration was poured into mild steel moulds which had been preheated at 400 °C accompanied with 30 s stirring process. The chemical compositions of the binary Mg–Zn and Mg–Ca–Zn alloys obtained by ICP-AES are listed in Table 1. Specimens of 15 mm × 15 mm × 10 mm size were cut from the achieved alloy ingots, and the samples were then mechanically wet ground with 320–4000 SiC grit papers. The morphology of specimens was studied by scanning electron microscopy (JEOL JSM-6380LA) equipped with EDS analysis. X-ray diffractometry (Siemens-D500) was used to evaluate the phases present in the specimens using Cu Kα line generated at 40 kV and 35 mA. To investigate the corrosion behavior in-vitro conditions, 15 mm × 15 mm × 10 mm samples were cut and mechanically ground by 320–2000 grit SiC sand paper. Afterward the ground samples were washed with distilled water, rinsed, and degreased ultrasonically with ethanol, then dried at room temperature for immersion test. The specimens were then immersed in a beaker containing 200 mL of Kokubo SBF. The Kokubo SBF was prepared according to the previously reported method [16]. The average pH value of the SBF from three measurements was recorded during the soaking experiment after an interval of 12 h. The corrosion rate (C_R) was calculated according to the previously reported method [8]. The potentiodynamic polarization in Kokubo solution was applied at pH 7.66 at 37 °C under air atmosphere for electrochemical test. The counter electrode material was graphite, the specimen was working electrode and the reference electrode was saturated calomel electrode (SCE). The potential scanning rate was fixed at 0.5 mV/s for all the specimens by initial potential at −250 mV below the open circuit potential. The exposed area of the specimens, which faced the Kokubo solution, was 1.5 cm^2. Each experiment was repeated twice to verify the reproducibility of the results. All potentials were in reference to the SCE.

3 Results and discussion

3.1 Microstructure characterization

The SEM observations of the alloys are illustrated in Fig. 1, showing the single-phase in pure Mg sample (α-Mg) (Fig. 1a).

When 1.25 wt.% Zn was added to the pure Mg, the microstructure of binary Mg–Zn alloys consisted of α-Mg and Mg$_{12}$Zn$_{13}$ secondary phases. Further addition of Zn up to 4 wt.% in Mg–Zn alloys leads to formation of large number of secondary phases (Mg$_{12}$Zn$_{13}$) in the microstructure. As can be seen in Fig. 1b and c the amount of the secondary phases in the grain boundary increased with increasing of the Zn content from 1.25 to 4 wt.% which was further confirmed by XRD pattern (Fig. 2a). The corresponding EDS analysis suggests that the dark area which is composed of Mg and Zn is related to Mg$_{12}$Zn$_{13}$ phase evolution (Fig. 1c). This result is in good agreement with binary Mg–Zn phase diagram (Fig. 3a).

In the Mg–Ca system, the maximum solubility of calcium in magnesium is 1.34 wt.% at room temperature in the equilibrium state [17]. Beyond this value Mg$_2$Ca phase starts to precipitate within the α-Mg matrix and at the grain boundary. However, in non-equilibrium state Mg$_2$Ca precipitates at lower calcium solubility, hence the microstructure of Mg–0.8Ca is composed of Mg matrix and Mg$_2$Ca intermetallic phase which precipitated within the grain boundary suggesting the evolution of eutectic phase (α-Mg + Mg$_2$Ca) (Fig. 1d). The EDS analysis showed that the triple junction of the grain boundaries were enriched with calcium which indicated the formation of Mg$_2$Ca phase within the grain boundaries (Fig. 1d). The addition of 1.25 wt.% Zn into Mg–0.8Ca led to the formation of α-Mg, IM1 and traces of Mg$_2$Ca phases since the atomic ratio of Zn/Ca was less than 1.25 (Fig. 1e).

The IM1 compound has the Ca$_3$Mg$_x$Zn$_{15-x}$ ($4.6 \leq x \leq 12$) formula at 335 °C. This compound has hexagonal structure with P6$_3$/mmc (194) space group and Sc$_3$Ni$_{11}$Si$_4$ prototype. The IM1 compound forms substitutional solid solution where Mg substitutes Zn atoms while Ca content remains constant at 16.7 at.%. The minimum and maximum solid solubility limits of the IM1 ternary compound determined by EPMA are 35.31 at.% Mg and 65.20 at.% Mg, respectively [18].

EDS analysis of Mg–0.8Ca–2.5Zn suggested the formation of lamellar eutectic phase (α-Mg + IM1 + Mg$_2$Ca) within the grain boundaries which is further confirmed by XRD pattern (Fig. 2b). This result is in good agreement with ternary Mg–Ca–Zn phase diagram (Fig. 4a). Further addition of Zn to 2.5 and 4 wt.% into the Mg–0.8Ca alloy resulted in the disappearance of Mg$_2$Ca intermetallic phase when the atomic ratio of Zn/Ca is greater than 1.25 (Fig. 1f). Thus the alloys microstructure is composed of α-Mg and IM1 compound. The amount of the secondary phase

Table 1. Chemical compositions of the binary Mg–xZn and ternary Mg–Ca–xZn alloys

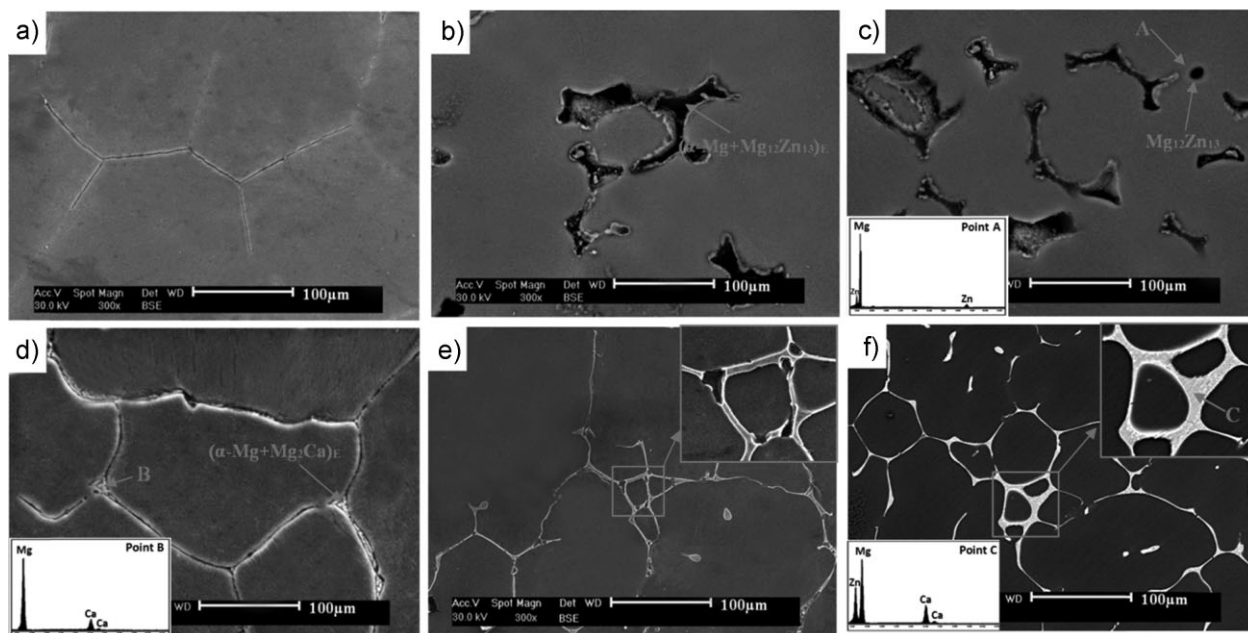| Alloy	Analysed compositions (wt.%)						
	Si	Zn	Ca	Mn	Al	Fe	Mg
Pure Mg	0.039	—	—	0.022	0.029	0.010	Bal.
Mg–1.25Zn	0.029	1.289	—	0.043	0.022	0.008	Bal.
Mg–2.5Zn	0.033	2.478	—	0.032	0.018	0.010	Bal.
Mg–4Zn	0.025	4.124	—	0.028	0.024	0.009	Bal.
Mg–0.8Ca–1.25Zn	0.038	1.324	0.831	0.024	0.023	0.008	Bal.
Mg–0.8Ca–2.5Zn	0.039	2.446	0.852	0.045	0.018	0.009	Bal.
Mg–0.8Ca–4Zn	0.028	4.210	0.840	0.037	0.027	0.007	Bal.

Figure 1. SEM micrographs of (a) pure Mg, (b) Mg–1.25Zn, (c) Mg–4Zn, (d) Mg–0.8Ca, (e) Mg–0.8Ca–1.25Zn, and (f) Mg–0.8Ca–2.5Zn

increased with the increase of Zn content within the grain boundaries, and the width of the grain boundary in Mg–0.8Ca–2.5Zn alloy was significantly thicker than that of Mg–0.8Ca–1.25Zn alloy. This phenomenon indicated the formation of a large amount of eutectic phase consisting of α-Mg and IM1 in the grain boundary. Addition of 4 wt.% Zn into the binary Mg–0.8Ca alloy led to the formation of α-Mg, IM1, and IM3 compounds. The IM3 compound has the $Ca_xMg_yZn_z$ ($8.2 \leq x \leq 9.1$; $27.1 \leq y \leq 31.0$; $60.8 \leq z \leq 64.7$) composition range at 335 °C. This compound has hexagonal structure with $P6_3/mmc$ (194) space group and $Sm_3Mg_{13}Zn_{30}$ prototype [19].

The calculated Mg–Zn binary system and phase assemblage diagram of Mg–xZn alloys are shown in Fig. 3. Similar types of phases are observed in all the Mg–xZn alloys but with different relative amounts as can be seen in Fig. 3b–d. 100 g of these alloys

is composed of ~1.25 to 4 g $Mg_{12}Zn_{13}$ at room temperature. Solidification of the binary Mg–Zn alloy starts with the formation of α-Mg at 640 °C while $Mg_{12}Zn_{13}$ secondary phase precipitates at 508 °C. Fig. 4 shows the calculated isothermal section of the Mg–Ca–Zn system at 335 °C, vertical section with constant 0.8 wt.% Ca and phase assemblage diagram of Mg–0.8Ca–xZn alloys. As can be seen from Fig. 4b when 1.25 wt.% Zn is added, the ternary alloy contains Mg_2Ca and IM1 compounds. In this case, a 100 g of the overall material, at room temperature, is composed of 95 g α-Mg, 4.5 g IM1, and 0.5 g Mg_2Ca (Fig. 4c). Based on this calculation, α-Mg starts to solidify at 640 °C and Mg_2Ca secondary phase starts to precipitate at 490 °C. However, the IM1 as a third phase starts to precipitate at 325 °C. When 2.5 wt.% Zn is added to the ternary alloy, Mg_2Ca does not form hence a 100 g of the overall material, at room
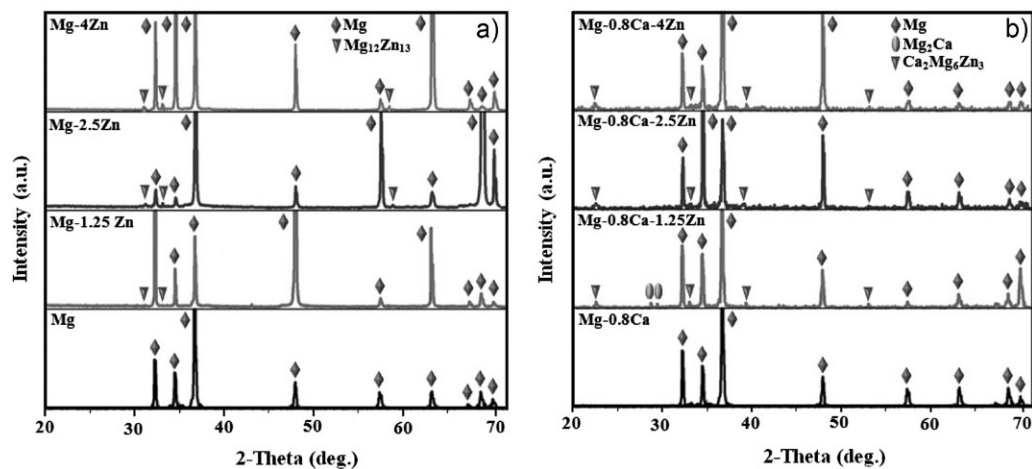

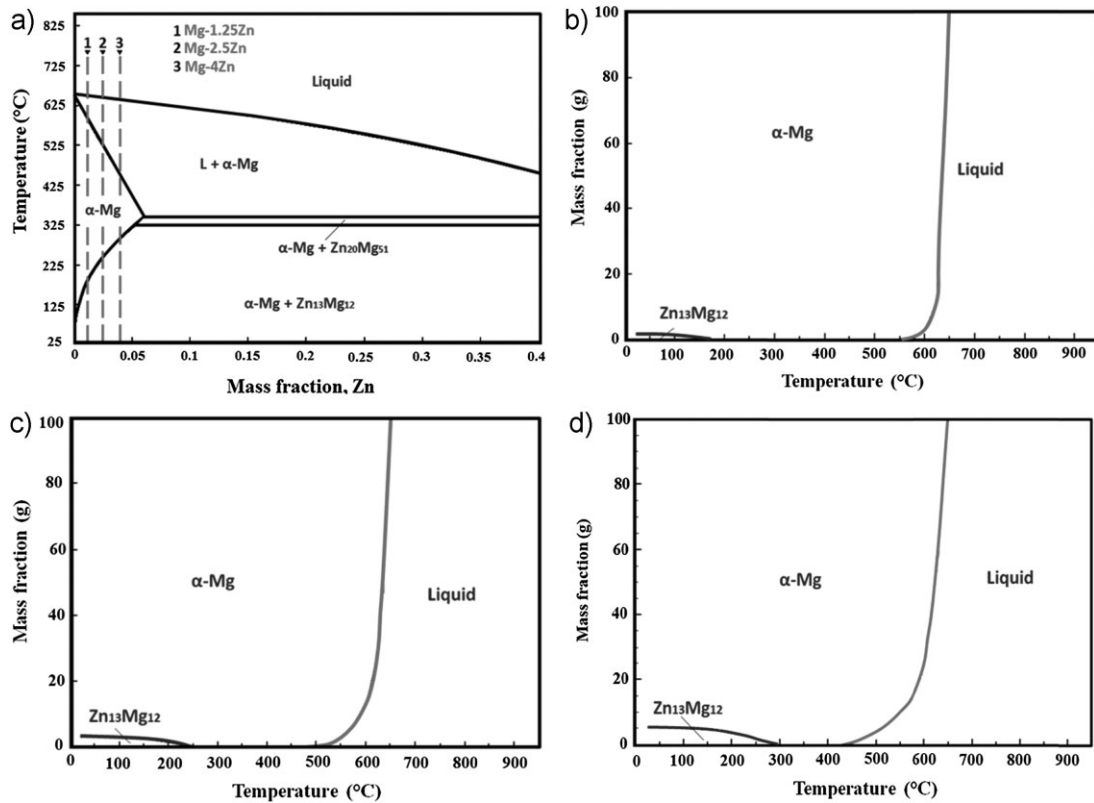**Figure 2.** XRD patterns of (a) Mg–xZn and (b) Mg–Ca–xZn alloys

Figure 3. (a) Calculated Zn-rich side of the Mg–Zn phase diagram and phase assemblage diagram of (b) Mg–1.25Zn, (c) Mg–2.5Zn, and (d) Mg–4Zn alloys
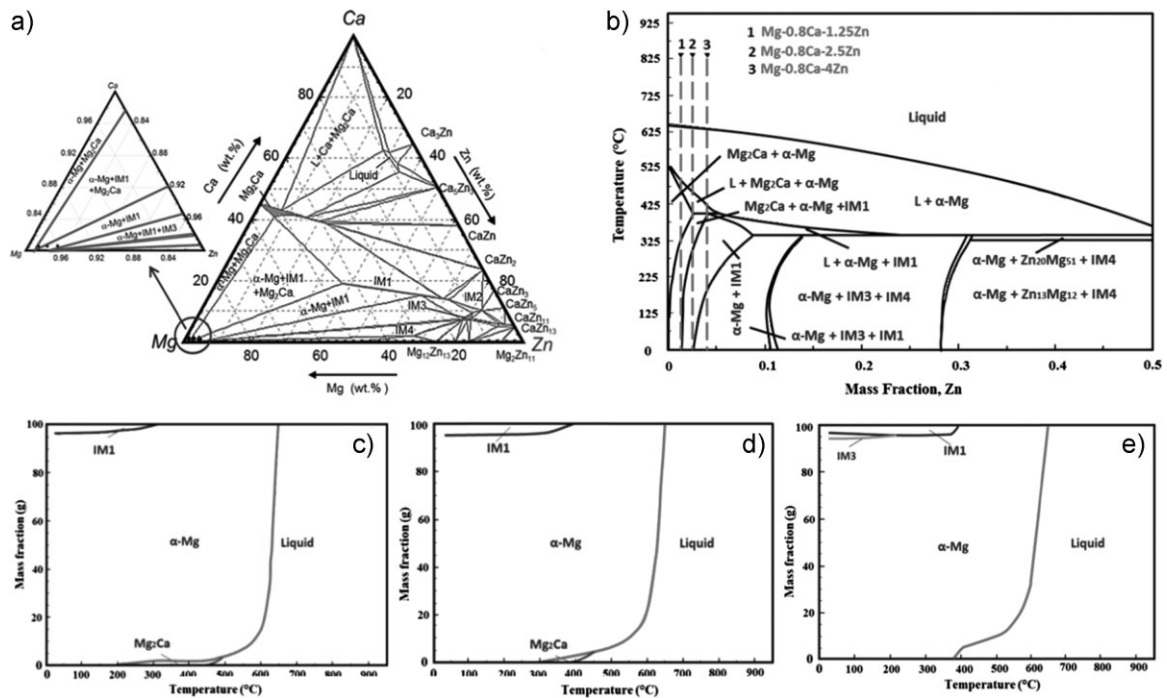

Figure 4. (a) Isothermal section of the Mg–Ca–Zn system at 335 °C [19], (b) calculated vertical section of the Mg–Ca–Zn system at 0.8 wt.% Ca and phase assemblage diagram of (c) Mg–0.8Ca–1.25Zn, (d) Mg–0.8Ca–2.5Zn, and (e) Mg–0.8Ca–4Zn alloys

temperature, is composed of 95 g Mg and 5 g IM1 compound (Fig. 4d). In this case α-Mg solidifies at 636 °C and IM1 starts to precipitate at 397 °C. The new IM3 compound was detected beside the α-Mg phase and IM1 compound in Mg–0.8Ca–4Zn alloy, hence a 100 g of the overall material is composed of 94 g Mg, 4 g IM1, and 2 g IM3 compounds (Fig. 4e). The α-Mg starts to solidify at 632 °C while, IM1 and IM3 start to precipitate at 397 and 190 °C, respectively.

3.2 Electrochemical measurements

Figure 5 displays the polarization curves recorded after 1 h exposure to Kokubo's solution for Mg–xZn, Mg–0.8Ca and Mg–Ca–xZn alloys. As can be seen Mg–0.8Ca has more negative corrosion potential compared to Mg–1.25Zn and Mg–0.8Ca–1.25Zn alloys indicating significant effect of Zn on the corrosion behavior of the alloy. The corrosion potential of Mg–0.8Ca was –1897.2 mV$_{SCE}$ which was relatively about 187 and 213 mV$_{SCE}$ lower than that of the Mg–1.25Zn and Mg–0.8Ca–1.25Zn alloys, respectively. By addition of 2.5 wt.% Zn, the binary Mg–Zn corrosion potential shifted toward nobler direction. Similar addition to the ternary Mg–Ca–Zn alloys showed the reverse effect. It was obvious from the polarization curves that, all binary Mg–xZn alloys have more positive corrosion potential compared to pure Mg. The corrosion current density of the Mg–0.8Ca–1.25Zn alloy was 180.4 µA/cm^2, lower than that of Mg–1.25Zn (212.4 µA/cm^2) and of Mg–0.8Ca (195.5 µA/cm^2). It indicates that the intermetallic phases have considerable effect on the corrosion rate of the alloy. The kinetics of cathodic reaction in Mg–0.8Ca and Mg–1.25Zn alloys are faster compared to Mg–0.8Ca–1.25Zn alloy. This phenomenon indicates that the cathodic reaction was kinetically more difficult in the ternary alloys compared to the binary alloys. Addition of 2.5 wt.% Zn, into the binary Mg–0.8Ca leads to a shift in the corrosion potential in a negative direction (−1721.1 mV$_{SCE}$) and increased corrosion current density to (222.3 µA/cm^2). Similar trend was observed when 4 wt.% Zn was added into the ternary alloy, as the corrosion potential shifted to −1747.7 mV$_{SCE}$ and corrosion current density increased to 317.8 µA/cm^2. This indicated lower corrosion resistance of Mg–0.8Ca–4Zn compared to the Mg–0.8Ca–1.25Zn alloy and Mg–

4Zn. From Fig. 5, it can be also seen that the hydrogen evolution (cathodic polarization) in the Mg–1.25Zn is higher than the other Mg alloys with more Zn content indicating the corrosion potential (E$_{corr}$) is more negative (active) in 1.25 wt.%. Zn. This can be due to the lack of Zn oxide layer on the surface of the alloy. The kinetics of cathodic reaction in Mg–1.25Zn is noticeably faster compared to other alloys with a lower percentage of Zn content. It can be suggested that in the galvanic coupling of Mg–4Zn, the α-Mg phase is assumed as the anode and the Mg$_{12}$Zn$_{13}$ phase is the cathode. Addition of the 4 wt.% Zn into the binary alloy leads to kinetic decrease in the cathodic and anodic reactions compared to other concentrations of Zn. This can be attributed to the fact that Zn forms a protective film on the surface of Mg–Zn alloys during corrosion process [20]. It is clear that Mg–4Zn alloy shows the lowest anodic current and highest corrosion potential, which presented the highest corrosion resistance among the binary alloys. The corrosion current density (i_{corr}), corrosion potential (E_{corr}, V$_{SCE}$), cathodic Tafel slopes (β_c), anodic Tafel slopes (β_a) and corresponding corrosion rate (P_i) extracted from the polarization curves are shown in Table 2. Also from the specimens' electrochemical parameters (i_{corr}, β_a, and β_c), polarization resistance (R_P) was calculated according to the following equation [20,21]:

$$R_P = \frac{\beta_a \beta_c}{2.3(\beta_a + \beta_c)i_{corr}} \tag{1}$$

The corrosion resistance of the binary Mg–Zn alloy enhanced as R_P values increased with the addition of Zn up to 4 wt.%. The addition of 1.25 wt.% Zn into the pure Mg increased the R_P from 0.82 to 1.09 kΩ cm^2. Further addition of Zn up to 4 wt.% leads to further increase in R_P value to 1.33 kΩ cm^2. The corrosion current density, i_{corr} (µA/cm^2), is related to the corrosion rate, P_i through the following empirical equation [22,23]:

$$P_i = 22.85\, i_{corr} \tag{2}$$

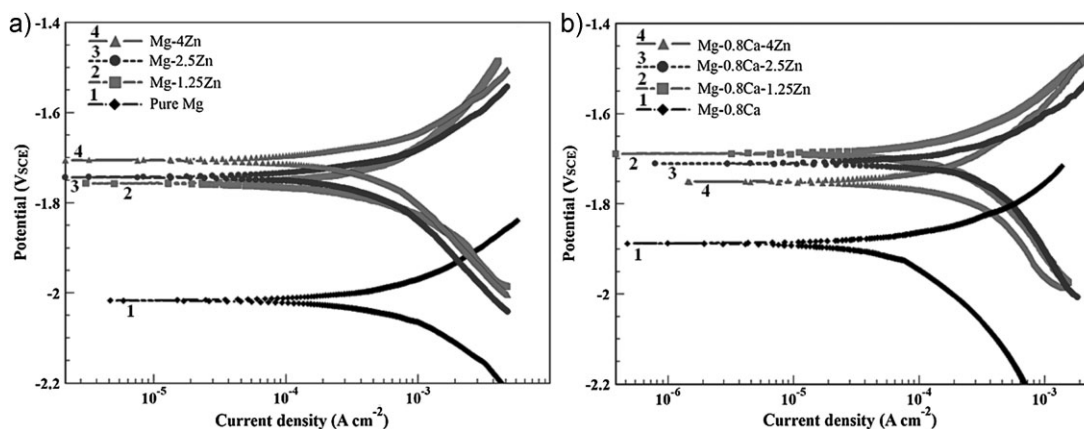According to Equation (2) the corrosion rate of the binary Mg–Zn alloys were increased in the order of Mg–4Zn < Mg–

Figure 5. Potentiodynamic polarization curves for: (a) Mg–xZn and (b) Mg–Ca–xZn alloys in Kokubo solution

Table 2. Electrochemical parameters of Mg–xZn and Mg–Ca–xZn alloys in Kokubo solution obtained from the polarization test

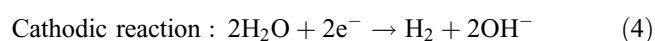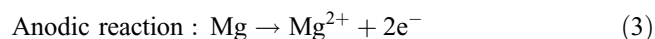| Alloy	Corrosion potential, E_{corr} (mV *vs*. SCE)	Current density, i_{corr} (μA/cm^2)	Cathodic slope, β_C (mV/decade) *versus* SCE	Anodic slope, β_a (mV/decade) *versus* SCE	Polarization resistance, R_P (kΩ cm^2)	Corrosion rate, P_i (mm/year)
Pure Mg	−2027.4	370.7	221.7	105.2	0.82	8.47
Mg–1.25Zn	−1762.6	282.7	237.5	101.3	1.09	6.45
Mg–2.5Zn	−1744.5	242.5	227.7	98.6	1.23	5.54
Mg–4Zn	−1710.6	212.4	212.1	91.7	1.31	4.85
Mg–0.8Ca	−1897.2	195.5	175.3	71.8	1.13	4.46
Mg–0.8Ca–1.25Zn	−1684.3	180.4	121.4	132.7	1.53	4.12
Mg–0.8Ca–2.5Zn	−1721.1	222.3	117.7	172.6	1.36	5.07
Mg–0.8Ca–4Zn	−1747.7	317.8	94.5	312.3	0.99	7.26

0.8Ca < Mg–2.5Zn < Mg–1.25Zn < Mg. The main reason for such improvement of corrosion resistance after addition of 4 wt.% Zn into the pure Mg can be due to the formation of more Zn oxides as an inner layer where the Mg (OH)$_2$ act as top layer. In the galvanic couple of Mg–0.8Ca alloy, the Mg$_2$Ca phase is assumed as the anode and the α-Mg phase is the cathode. This can be due to high electrochemical activity of Mg$_2$Ca compared to α-Mg. However, ternary Mg–0.8Ca–1.25Zn alloy is composed of α-Mg, Mg$_2$Ca, and IM1 phases. Thus in these alloys, IM1 phase acts as the cathode and Mg$_2$Ca phase acts as the anode. It can be concluded that Mg$_2$Ca phase was more reactive (corroded faster) than that of IM1 and α-Mg phases, while, IM1 phase was less active than α-Mg. In the alloys containing 2.5 wt.% Zn, the IM1 and α-Mg phases act as the cathode and the anode respectively. However, by increasing Zn content up to 4 wt.% into the alloy IM3 formed in addition to IM and α-Mg. Therefore the galvanic couple occurred between IM1 and IM3 phases where IM1 phase is the cathode and IM3 phase is the anode.

The reason for the reduced corrosion resistance of Mg–0.8Ca–1.25Zn alloy compared to other ternary alloys was due to the presence of IM1 phase. Polarization resistance further confirmed the higher R_p value of Mg–0.8Ca–1.25Zn (1.53 kΩ cm^2) compared to other ternary alloys and binary Mg–0.8Ca alloy (1.13 kΩ cm^2). In the galvanic couple of the Mg–0.8Ca–1.25Zn alloy, Mg$_2$Ca phase corroded extensively but the IM1 phase interrupted the formation of the continuous network structure of Mg$_2$Ca phase reducing the effect of galvanic couples significantly, thus improving the corrosion resistance. However, further addition of Zn up to 4 wt.% into the ternary alloy leads to increase the corrosion rate due to the occurrence of more galvanic corrosion between α-Mg, IM1, and IM3 phase. This can be attributed to the anodic action of α-Mg phase against the cathodic action of IM1 phase which leads to the α-Mg phase corroding quickly and almost disappearing while, IM1 phase remained in the structure. Therefore α-Mg cannot further support the IM1 phase and corrosion resistance decreased significantly.

3.3 Immersion test

Figure 6 shows SEM corrosion morphologies of Mg–Zn and Mg–Ca–Zn alloy specimens after immersion in Kokubo solution for

144 h. Fig. 6a revealed the formation of cracks accompanied by non-uniform distribution and large amount of the precipitates which deposited on the crack layer of the Mg–1.25Zn alloy. By increasing the Zn content to 2.5 wt.% into binary Mg–Zn alloy, the number of cracks decreased and small amount of particles precipitated on the crack layer as shown in Fig. 6b. The main reason for crack formation is the dehydration of the layer after drying in ambient atmosphere [21]. EDS analysis Fig. 6g shows that the precipitate is composed of high amounts of Mg and O, as well as low amount of Ca and P (point 1). The mole ratio of O to Mg was about 2.03 which indicated the formation of magnesium hydroxide Mg(OH)$_2$. However, the EDS analysis of the precipitate (point 2) exhibited the presence of magnesium, calcium, phosphorus, oxygen, and carbon elements which implied the formation of hydroxyapatite (HA) (Fig. 6g). It was obvious from Fig. 6c that the uniform corrosion product precipitates on the surface of Mg–4Zn alloy. The tiny cracks formed during the immersion test are due to the previously mentioned water loss of the corrosion products. However, in the ternary Mg–0.8Ca–1.25Zn alloy, corrosion products precipitated on the crack layer (Fig. 6d), and the EDS analysis from point 3 showed the corrosion product consisted of C, O, P, Mg, and Ca which represent the formation of HA (Fig. 6h). These products acted as barrier films to protect the surface from aggressive solution and thus enhanced corrosion resistance [16]. Adding 2.5 wt.% of Zn to the Mg–0.8Ca alloy caused the formation of thick network-like cracks and precipitates evenly distributed on the entire surface of the alloy (Fig. 6e). The EDS analysis of precipitates is exhibited in Fig. 6h. Further addition of Zn to 4 wt.% into the ternary alloy leads to precipitate more particles on the crack layer accompanied with the formation of a deep pit on the surface of the alloy (Fig. 6f). In general, Mg and its alloys are reactive when exposed to the SBF, thus Mg^{2+} rich interface is generated and the extra Mg^{2+} ions at the interface between the solution and the sample serve to prevent the nucleation of calcium phosphate deposition. The formation of corrosion product follows the following reactions:
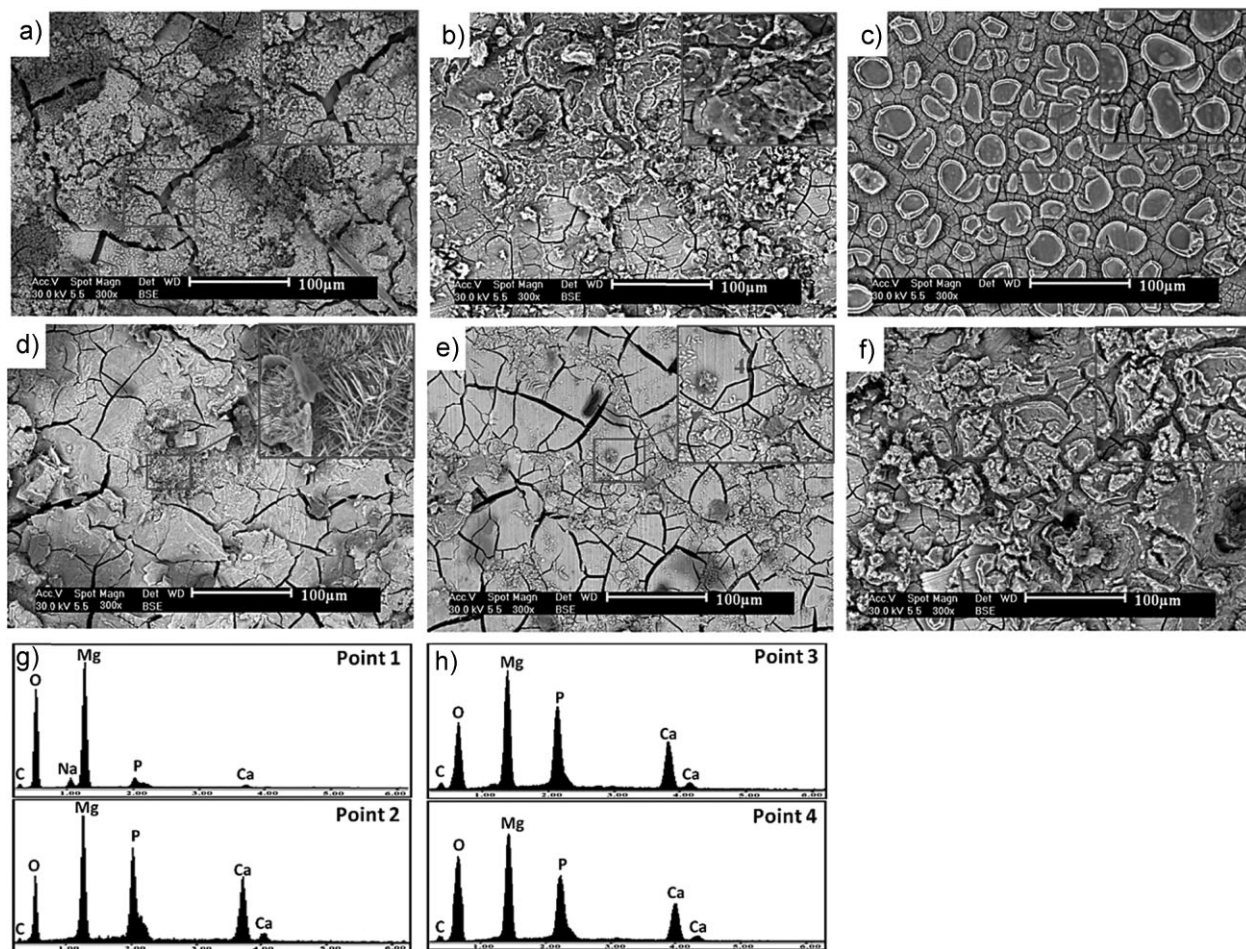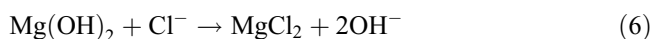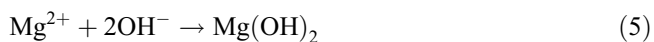
$$\text{Anodic reaction : } Mg \rightarrow Mg^{2+} + 2e^- \tag{3}$$

$$\text{Cathodic reaction : } 2H_2O + 2e^- \rightarrow H_2 + 2OH^- \tag{4}$$

Figure 6. SEM micrographs of binary Mg–xZn alloy with various Zn content: (a) 1.25, (b) 2.5, (c) 4, and ternary Mg–Ca–xZn alloys with various Zn content (d) 1.25, (e) 2.5, (f) 4 wt.%, (g) EDS analyses of point 1, 2, and (h) point 3, 4 after immersion into Kokubo for 144 h duration

$$Mg^{2+} + 2OH^- \rightarrow Mg(OH)_2 \qquad (5)$$

$$Mg(OH)_2 + Cl^- \rightarrow MgCl_2 + 2OH^- \qquad (6)$$

Mg transforms to stable Mg^{2+} ions, subsequently the cathodic reaction occurs at the same time by formation of hydroxide ion according to reactions (3) and (4). The Mg^{2+} ions react with hydroxide ions and form magnesium hydroxide [21]. By evolution of $Mg(OH)_2$ as a barrier layer, the degradation rate of the sample declines and corrosion products such as CO_3^{2-}, PO_4^{3-}, and Cl^- ions are precipitated on the surface of the specimen [23]. Regarding Equation (6), chloride ion reacts with the deposed $Mg(OH)_2$ on the specimens and forms $MgCl_2$ having higher solubility compared to $Mg(OH)_2$. The Cl^- ion can decrease the corrosion resistance of the specimens. Moreover, Cl^- ion can easily penetrate the deposited layer due to its small radius which caused the preferential adsorption and the OH^- replacement [24]. As the reaction progresses, high amounts of Mg^{2+} are dissolved, thus more HCO_3^-, HPO_4^{2-}, and Ca^{2+} in the solution reacted with OH^- to form HA which cause a decrease in the corrosion rate.

The pH variation of the SBF for Mg–Zn and Mg–Ca–Zn alloys as a function of immersion time are shown in Fig. 7. From the graph it is obvious that the pH values of the binary Mg–Zn alloys increased from about 7.66 to 9.50 (Fig. 7a), while ternary alloys increased from about 7.66 to 8.90 at the early stage of immersion test (Fig. 7b). An early increase in pH values for specimens was caused by accumulation of OH^- ion in the form of $Mg(OH)_2$ on the surfaces of the specimens [16]. By increasing the immersion time to 144 h, the pH value of binary Mg–Zn alloys gradually increased to around 9.70 representing a constant trend. This phenomenon is due to the formation of $Mg(OH)_2$ and the precipitation of calcium phosphate as a top layer on the $Mg(OH)_2$. At the same time, by consuming the calcium phosphate from the solution, the amount of hydroxyapatite precipitation on the surface increased. Similar trend is also observed for the ternary Mg–Ca–Zn alloys where pH values steadily increased to around 9.50.

Figure 8 illustrates the XRD pattern of Mg–xZn and Mg–Ca–xZn alloys after 144 h immersion in Kokubo solution. The patterns indicate the presence of $Mg(OH)_2$ accompanied by Mg and HA. The pure Mg specimens show broader $Mg(OH)_2$ peaks as main corrosion products than those of Mg–1.25Zn, Mg–2.5Zn
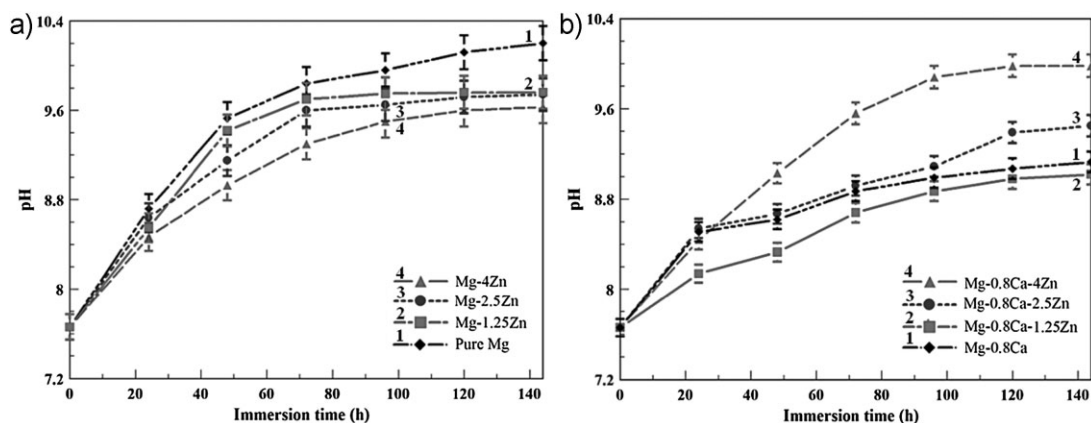
Figure 7. Variation of the pH value in Kokubo solution as a function of immersion time of (a) Mg–*x*Zn and (b) Mg–Ca–*x*Zn for duration of 144 h

and Mg–4Zn alloys. Furthermore, it was observed that the diffraction intensities of $Mg(OH)_2$ decreased with increasing Zn content (Fig. 8a). Highest intensity of $Mg(OH)_2$ peaks was detected in the case of pure Mg. It is suggested that a considerable amount of $Mg(OH)_2$ was formed on the surface of the specimens. The presence of $Mg(OH)_2$ in the corrosion products of Mg–0.8Ca alloy can also be seen (Fig. 8b). However, the less significant

presence of HA was detected in the corrosion products of this alloy. After addition of 1.25 wt.% Zn into the binary Mg–0.8Ca alloy, the intensity of $Mg(OH)_2$ significantly decreased. The amount of $Mg(OH)_2$ in Mg–0.8Ca–2.5Zn alloys was higher than that of Mg–0.8Ca–4Zn alloys indicating lower corrosion attack. The XRD results also present the existence of lower amounts of $Mg(OH)_2$ in corrosion products of ternary Mg–0.8Ca–1.25Zn
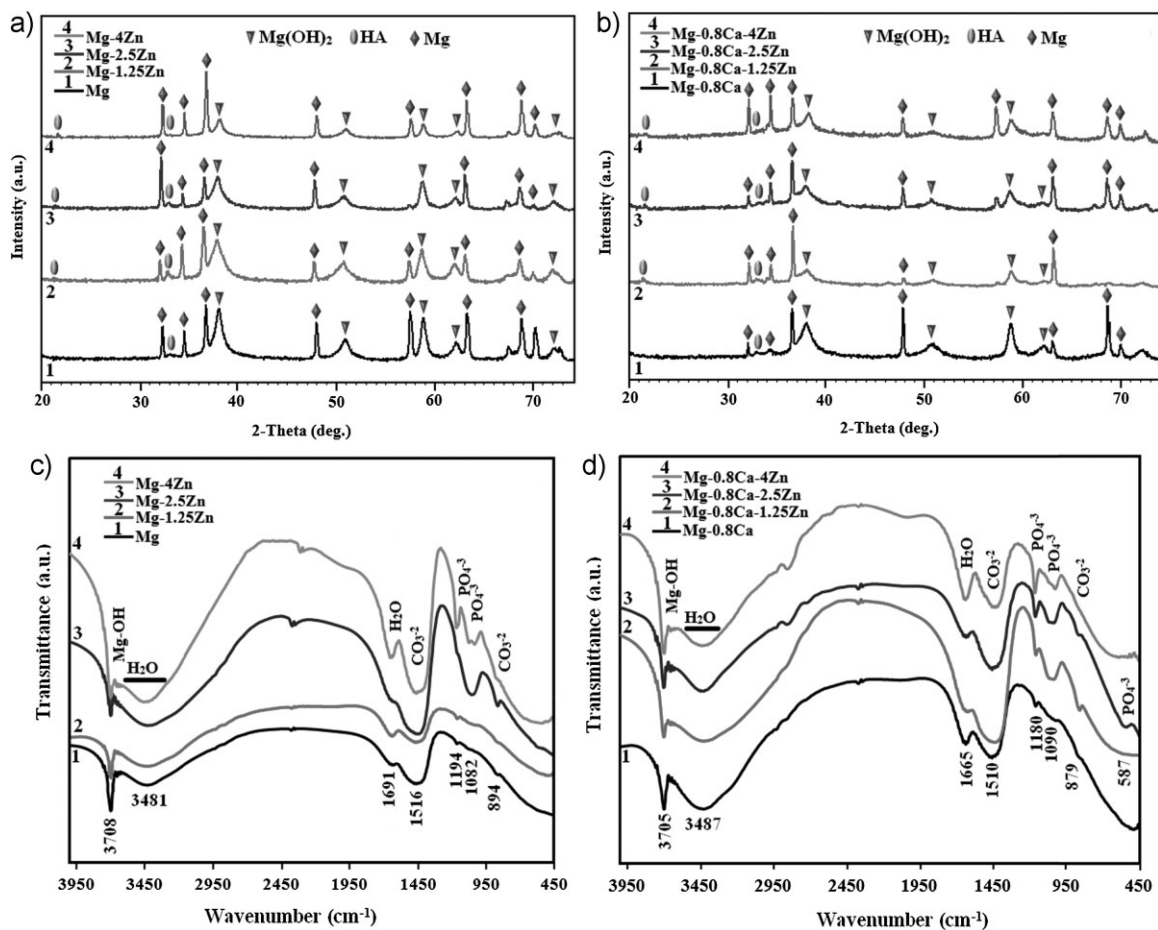

Figure 8. X-ray diffraction of (a) Mg–*x*Zn, (b) Mg–Ca–*x*Zn and FTIR absorption spectra of (c) Mg–*x*Zn, and (d) Mg–Ca–*x*Zn after full immersion exposure to Kokubo solution for 144 h duration
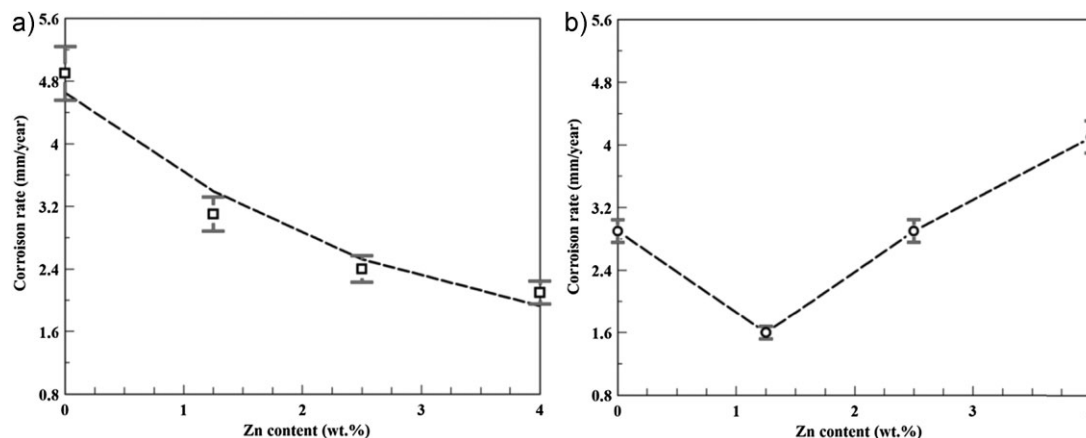
Figure 9. Corrosion rate obtained by weight loss for (a) Mg–xZn and (b) Mg–Ca–xZn as a function of Zn content in Kokubo solution for 144 h

alloys compared to the Mg–1.25Zn alloys. Porous $Mg(OH)_2$ formed at the initial stage of the corrosion process acts as a protective film for the precipitation of Ca and P. However the presence of Cl^- ions contributes to the breakdown of the $Mg(OH)_2$ film thus prompting pit formation [25]. Therefore it is crucial to suppress formation of $Mg(OH)_2$ on the surface of the alloy for deposition of calcium phosphate. The FTIR spectra of corrosion products for pure Mg and Mg–xZn alloys in Fig. 8c showed very strong and sharp peak at $3708\,cm^{-1}$. This characteristic is identified as the O–H stretching in the crystal structure of $Mg(OH)_2$. The broad absorption band at $3481\,cm^{-1}$ is attributed to the vibration of water molecules. The band at $1691\,cm^{-1}$ is also attributed to water vibration. Phosphate group (PO_4^{3-}) was detected around $1194–1082\,cm^{-1}$ for the ν_3 mode. A band at $894\,cm^{-1}$ is assigned to ν_2 vibration mode of carbonated (CO_3^{2-}) groups. It is evident that the corrosion products on the surface of pure Mg and Mg–xZn alloys mainly consist of $Mg(OH)_2$ and HA. However, the absorbance of the spectra from the $Mg(OH)_2$ as a main corrosion product decreased with increasing Zn content. The presence of $Mg(OH)_2$ in the corrosion product of pure Mg and Mg–xZn alloys, was further confirmed via XRD results. The FTIR spectrum of corrosion products of Mg–0.8Ca and Mg–0.8Ca–xZn alloys (Fig. 8d) showed similar absorption band characteristic for three types of bond-stretching including hydroxyl, carbonate and phosphates group in the functional group region. Overall the kind of corrosion products formed on the surface of pure Mg, binary Mg–0.8Ca, Mg–xZn and ternary Mg–0.8Ca–xZn alloys were similar but their amounts were different.

Figure 9 exhibits the average mass loss of binary Mg–xZn and ternary Mg–Ca–xZn alloys as a function of immersion in Kokubo solution for 168 h. The average corrosion rate of pure Mg and Mg–1.25Zn was 4.91 and 3.17 mm/year, respectively. However, these values decrease to 2.14 mm/year in Mg–4Zn alloy (Fig. 9a). In the Mg–Zn samples, $Mg(OH)_2$ is located in the surface layer as top layer while Zn oxide is located in the inner layer. This phenomenon is because Zn is less chemically active compared to Mg hence magnesium is oxidized first and forms on the surface of the alloy. The oxide film on Mg–4Zn is much thicker compared to the Mg–2.5Zn and Mg–1.25Zn which can be

attributed to the influence of Zn content. The binary Mg–0.8Ca alloy shows higher degradation rate (2.87 mm/year) than that of Mg–0.8Ca–1.25Zn alloys. Addition of 4 wt.% Zn in the ternary alloy accelerates the degradation rate to 4.13 mm/year indicating serious corrosion attack on the alloy (Fig. 9b). As the Zn content decreases to 1.25 wt.%, the degradation rate drops to the lowest value (1.62 mm/year). Uniform distribution of IM1 and Mg_2Ca along the grain boundaries that acted as obstacles for electron transfer from α-Mg phase to another phase leads to fewer hydrogen bubbles surrounding the Mg–0.8Ca–1.25Zn sample compared to the other alloys. This phenomenon led to further electron transfer resistance between α-Mg phase and the intermetallic phases. This resulted in the reduction of the effective driving force for galvanic corrosion causing a decline in the corrosion rate [26].

4 Conclusions

In the present study, the microstructure and bio-degradation behavior of binary and ternary Mg based alloys with various Zn content were investigated. In the binary Mg–Zn alloys the type of secondary phase ($Mg_{12}Zn_{13}$) is constant but the amount at grain boundaries increased with increasing Zn content up to 4 wt.%. In the ternary Mg–Ca–Zn alloys, the type of the secondary phases changed according to the Zn/Ca atomic ratio while their amount increased with increasing of Zn content. Four different phases were observed in the ternary alloys; α-Mg, Mg_2Ca, IM1 and IM3. However in the binary alloys only two phases were detected; α-Mg and $Mg_{12}Zn_{13}$. Polarisation test showed that corrosion rates of Mg–xZn alloys decreased significantly with increasing Zn content. Corrosion rates of Mg–Ca–xZn alloys decreased with increasing Zn content up to 1.25 wt.%. However, further addition of Zn up to 4 wt.% increased the corrosion rates. Immersion tests in Kokubo solution showed that corrosion resistance of the binary Mg–Zn alloys is strongly related to the volume fraction of $Mg_{12}Zn_{13}$ and the amount of Zn oxide layer. However, this characteristic in the ternary Mg–Ca–Zn alloys depended on Zn/Ca ratio and the type of secondary phases.

5 References

[1] L. Chang, L. Tian, W. Liu, X. Duan, *Corros. Sci.* **2013**, *72*, 118.

[2] P. Rosemann, J. Schmidt, A. Heyn, *Mater. Corros.* **2013**, *64*, 4714.

[3] H. S. Brar, J. P. Ball, I. S. Berglund, J. B. Allen, M. V. Manuel, *Acta Biomater.* **2013**, *9*, 5331.

[4] G. Song, *Corros. Sci* **2007**, *49*, 1696.

[5] F. Witte, F. Feyerabend, P. Maier, *Biomaterials* **2007**, *28*, 2163.

[6] J. G. Li, Y. Lv, H. W. Wang, *Mater. Corros.* **2013**, *64*, 426.

[7] L.-Q. Wang, J.-S. Zhou, J. Liang, J.-M. Chen, *Mater. Corros.* **2013**, *64*, 1.

[8] L. Wang, T. Zhou, J. Liang, *Mater. Corros.* **2012**, *63*, 713.

[9] Y.-Q. Wang, M.-Z. Li, C. Li, X.-Y. Li, L.-Q. Fan, T. Jia, *Mater. Corros.* **2012**, *63*, 497.

[10] T.-H. Nam, S.-H. Kim, J.-G. Kim, S.-K. Kim, *Mater. Corros.* **2012**, *63*, 1.

[11] Z. Li, X. Gu, S. Lou, Y. Zheng, *Biomaterials* **2008**, *29*, 1329.

[12] N. Li, Y. Zheng, *J. Mater. Sci. Technol.* **2013**, *29*, 489.

[13] Y. Shi, M. Qi, Y. Chen, P. Shi, *Mater. Lett.* **2011**, *65*, 2201.

[14] H. Du, Z. Wei, X. Liu, E. Zhang, *Mater. Chem. Phys.* **2011**, *125*, 568.

[15] G. Ben-Hamu, D. Eliezer, *Mater. Corros* **2013**, *64*, 516.

[16] H. R. Bakhsheshi-Rad, M. H. Idris, M. R. A. Kadir, *Surf. Coat. Tech.* **2013**, *222*, 79.

[17] Alloy phase diagram, in: ASM Handbook, V.A.I., The Materials Information Company; **1992**.

[18] Y. N. Zhang, D. Kevorkov, J. Li, E. Essadiqi, M. Medraj, *Intermetallics* **2010**, *18*, 2404.

[19] Y. N. Zhang, D. Kevorkov, X. D. Liu, F. Bridier, P. Chartrand, M. Medraj, *J Alloys Compd.* **2012**, *523*, 75.

[20] G. R. Argade, K. Kandasamy, S. K. Panigrahi, R. S. Mishra, *Corros. Sci.* **2012**, *58*, 321.

[21] H. R. Bakhsheshi-Rad, M. R. Abdul-Kadir, M. H. Idris, M. Daroonparvar, *Trans. Nonferrous Met. Soc. China* **2013**, *23*, 699.

[22] Z. Shi, M. Liu, A. Atrens, *Corros. Sci.* **2010**, *52*, 579.

[23] H. R. Bakhsheshi-Rad, E. Hamzah, M. Medraj, M. H. Idris, M. Daroonparvar, A. F. Lotfabadi, M. A. M. Yajid, *Mater. Corros.* **2013**, doi: 10.1002/maco.201307492

[24] J. Wang, L. Wang, S. Guan, S. Zhu, C. Ren, S. Hou, *J. Mater. Sci. Mater. Med.* **2010**, 21, 2001.

[25] Y. Wang, M. Wei, J. Gao, *Mater. Lett.* **2008**, *62*, 2181.

[26] T. Lei, W. Tang, S. H. Cai, *Corros. Sci.* **2012**, *54*, 270.